

IONIZED GAS OUTFLOWS IN INFRARED-BRIGHT DUST-OBSCURED GALAXIES SELECTED WITH WISE AND SDSS

YOSHIKI TOBA^{1,2}, HYUN-JIN BAE^{3,4,5}, TOHRU NAGAO², JONG-HAK WOO³, WEI-HAO WANG¹, ALEXANDER Y. WAGNER^{6,7}, AI-LEI SUN^{1,8}, YU-YEN CHANG¹

¹Academia Sinica Institute of Astronomy and Astrophysics, PO Box 23-141, Taipei 10617, Taiwan

²Research Center for Space and Cosmic Evolution, Ehime University, Bunkyo-cho, Matsuyama, Ehime 790-8577, Japan

³Astronomy Program, Department of Physics and Astronomy, Seoul National University, Seoul 151-742, Korea

⁴Department of Astronomy and Center for Galaxy Evolution Research, Yonsei University, Seoul 120-749, Korea

⁵Biomedical engineering research center, Asan Medical Center, Seoul 05505, Korea

⁶Center for Computational Sciences, University of Tsukuba, 1-1-1 Tennodai, Tsukuba, Ibaraki 305-8577, Japan

⁷Institut d’Astrophysique de Paris 98 bis bd Arago, F-75014 Paris, France

⁸Department of Physics and Astronomy, Bloomberg Center, Johns Hopkins University, Baltimore, MD 21218, USA

ABSTRACT

We present the ionized gas properties of infrared (IR)-bright dust-obscured galaxies (DOGs) that show an extreme optical/IR color, $(i - [22])_{AB} > 7.0$, selected with the Sloan Digital Sky Survey (SDSS) and Wide-field Infrared Survey Explorer (*WISE*). For 36 IR-bright DOGs that show [O III] λ 5007 emission in the SDSS spectra, we performed a detailed spectral analysis to investigate their ionized gas properties. In particular, we measured the velocity offset (the velocity with respect to the systemic velocity measured from the stellar absorption lines) and the velocity dispersion of the [O III] line. We found that the derived velocity offset and dispersion of most IR-bright DOGs are larger than those of Seyfert 2 galaxies (Sy2s) at $z < 0.3$, meaning that the IR-bright DOGs show relatively strong outflows compared to Sy2s. This can be explained by the difference of IR luminosity contributed from active galactic nucleus, L_{IR} (AGN), because we found that (i) L_{IR} (AGN) correlates with the velocity offset and dispersion of [O III] and (ii) our IR-bright DOGs sample has larger L_{IR} (AGN) than Sy2s. Nevertheless, the fact that about 75% IR-bright DOGs have a large ($> 300 \text{ km s}^{-1}$) velocity dispersion, which is a larger fraction compared to other AGN populations, suggests that IR-bright DOGs are good laboratories to investigate AGN feedback. The velocity offset and dispersion of [O III] and [Ne III] λ 3869 are larger than those of [O II] λ 3727, which indicates that the highly ionized gas tends to show more stronger outflows.

Keywords: catalogs — galaxies: active — galaxies: kinematics and dynamics — infrared: galaxies

1. INTRODUCTION

It has been well-known that the mass of the super massive black hole (SMBH) tightly correlates with the properties of its host galaxy such as spheroid component mass and stellar velocity dispersion, which suggests that SMBHs and galaxies coevolve (so-called “co-evolution”: e.g., Magorrian et al. 1998; Marconi & Hunt 2003; Kormendy & Ho 2013; McConnell & Ma 2013; Sun et al. 2013; Woo et al. 2013). Observations at various wavelengths have indicated that radiation, winds, and jets from an active galactic nucleus (AGN)

can interact with the interstellar medium, and this can lead to the ejection or heating of gas. Therefore, AGN feedback has been increasingly considered as a key component to understand the galaxy formation and evolution (e.g., Fabian et al. 2012, and references therein), which is also supported by hydrodynamical simulations (e.g., Wagner & Bicknell 2011; Faucher-Giguère & Quataert 2012; Wagner et al. 2013; Bieri et al. 2017). These powerful outflows resulting from feedback caused by the AGN regulate star formation (SF) and even AGN activity, and could control co-evolution of galaxies and SMBHs (e.g., Di Matteo et al. 2005; Cano-Díaz, et al. 2012; King & Pounds 2015). Measuring the kinematics of

multiphase gas is one of the useful ways to investigate gas outflows in AGNs. In particular, the velocity offset of the $[\text{O III}] \lambda 5007\text{\AA}$ narrow emission and its velocity dispersion are good tracers for probing AGN-driven outflows. Many works have reported strong $[\text{O III}]$ outflows in AGNs (e.g., Zamanov et al. 2002; Aoki et al. 2005; Bian et al. 2005; Boroson 2005; Komossa et al. 2008; Crenshaw et al. 2010; Greene et al. 2011; Villar-Martín et al. 2011; Rodríguez Zaurín et al. 2013; Liu et al. 2013a,b; Mullaney et al. 2013; Zakamska & Greene 2014; Sun et al. 2017) and investigated their statistical properties (e.g., Wang et al. 2011; Bae & Woo 2014; Woo et al. 2016, 2017). The advent of the integral field unit (IFU) enables us to investigate AGN feedback providing spatial information of AGN outflows from local Universe (e.g., Barbosa et al. 2009; Harrison et al. 2014; McElroy et al. 2015; Karouzos et al. 2016b,b; Bae et al. 2017) to high- z Universe (e.g., Alexander et al. 2010; Brusa et al. 2015; Carniani et al. 2016).

In this paper, we present the ionized gas properties of IR-bright dust-obscured galaxies (DOGs: Dey et al. 2008; Toba et al. 2015) that show an extreme optical and IR color, i.e., their flux densities in the mid-IR (MIR) regime are about 1000 times brighter than those in the optical regime, indicating that these objects are undergoing strong AGN and/or SF activity behind the large amount of dust. We have performed IR-bright DOGs search and investigated their statistical and physical properties such as IR luminosity function (Toba et al. 2015), auto-correlation function (Toba et al. 2017a), and stellar mass and star-formation rate relation (Toba et al. 2017b). The IR luminosity of most of the IR-bright DOGs exceeds $10^{12}L_{\odot}$ or even $10^{13}L_{\odot}$, which are termed ultraluminous infrared galaxies (ULIRGs: Sanders & Mirabel 1996) and hyperluminous infrared galaxies (HyLIRGs: Rowan-Robinson 2000), respectively. In the context of major merger scenario, the gas accreting onto the nucleus triggers the AGN activity due to the merger process, and enormous energy originated from the AGNs then significantly affects SF activity in the host galaxies (e.g., Hopkins et al. 2006, 2008). Since IR-bright DOGs may correspond to a maximum phase of AGN activity behind large amount of dust (e.g., Narayanan et al. 2010), they are expected to be a good laboratory to investigate the AGN feedback phenomenon. Note that observations of molecular and atomic gas are quite useful to investigate the kinematics and energetics of outflowing gas (e.g., Ciccone et al. 2014). However, these investigations often require follow-up observations with radio telescopes and the sample size is limited due to the low efficiency of these observations. In order to investigate the statistical as-

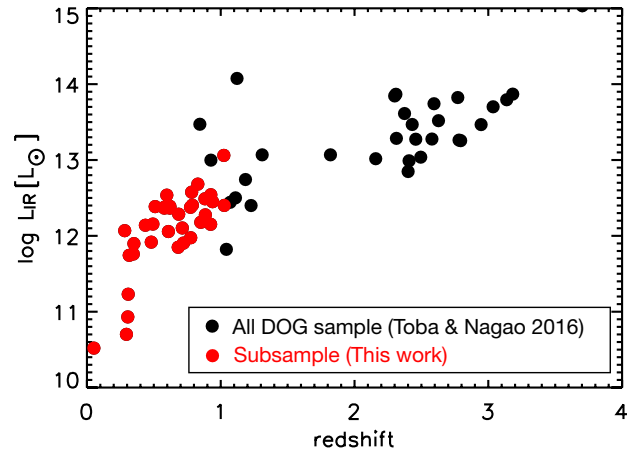


Figure 1. IR luminosity as a function of redshift for our IR-bright DOG sample, discovered by Toba & Nagao (2016). Red circles show objects that are used for the spectral analysis in this work.

pect of outflowing gas in IR-bright DOGs, we focus on ionized gas.

This paper is organized as follows. We describe the sample selection and spectral analysis in Section 2. The resultant outflow properties of $[\text{O III}]$ is presented in Section 3. In Section 4, we discuss the dependence of the $[\text{O III}]$ outflow properties on physical properties such as IR luminosity. We also discuss the energetics of AGN outflow in our sample and present the outflow properties of other emission lines. We summarize in Section 5. Throughout this paper, the adopted cosmology is a flat universe with $H_0 = 70 \text{ km s}^{-1} \text{ Mpc}^{-1}$, $\Omega_M = 0.3$, and $\Omega_{\Lambda} = 0.7$. Unless otherwise noted, all magnitudes refer on the AB system, and we adopt vacuum wavelengths for the analysis.

2. DATA AND ANALYSIS

The DOG Sample for the spectral analysis was selected from a IR-bright DOG sample in Toba & Nagao (2016). They selected 67 IR-bright DOGs with $(i - [22])_{AB} > 7.0$ and flux density at $22 \mu\text{m} > 3.8 \text{ mJy}$ from the Sloan Digital Sky Survey (SDSS) spectroscopic catalog (York et al. 2000; Alam et al. 2015) and *Wide-field Infrared Survey Explorer (WISE)* ALLWISE catalog (Wright et al. 2010; Cutri et al. 2014). Among them, we narrowed down to 36 objects with $0.05 < z < 1.02$ that clearly have $[\text{O III}]$ in their SDSS spectra¹. Figure 1 shows IR luminosity, L_{IR} ($8\text{--}1000 \mu\text{m}$), as a function of redshift for all IR-bright DOG sample and

¹ Within our sample, the spectra of SDSS1010+3775 (ID=12), SDSS1248+4242 (ID=21), SDSS1407+3601 (ID=26), and SDSS1513+1451 (ID=30) have also reported in Ross et al. (2015). They also mentioned that SDSS1010+3775 has unusually broad $[\text{O III}]$ with non-Gaussian structure.

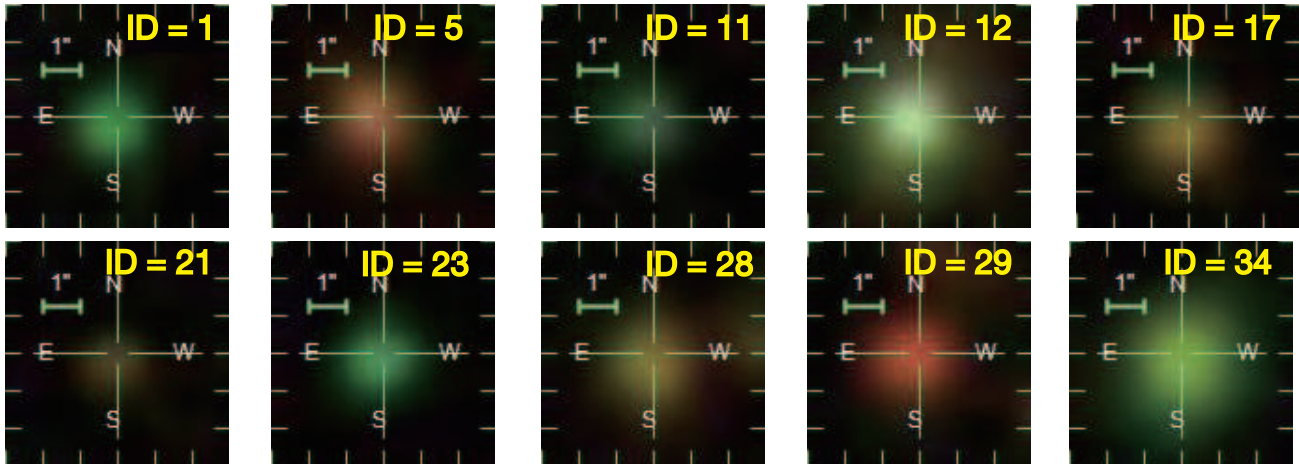


Figure 2. Example of the SDSS *gri*-composite images of our IR-bright DOG sample.

this subsample. The IR luminosities of the 36 IR-bright DOG sample are $\log L_{\text{IR}} [L_{\odot}] = 10.5 - 13.1$, and 25/36 ($\sim 69\%$) objects are classified as ULIRGs/HyLIRGs (see Table 1). Recently some authors have discovered many (obscured) ULIRGs/HyLIRGs based on the SDSS and *WISE* data and reported powerful ionized outflows seen in their spectra (Ross et al. 2015; Zakamska et al. 2016; Bischetti et al. 2017; Hamann et al. 2017; Zhang et al. 2017), although they basically focus on high- z ($z > 2$) objects.

The SDSS spectra for all 36 IR-bright DOGs are shown in Figure A1–A4 (see Appendix A). The mean full width at half maximum (FWHM) of their $H\beta$ line is about 503 km s^{-1} . When we adopt 1000 km s^{-1} as a threshold to discriminate between type 1 and 2 AGNs (e.g., Yuan et al. 2016), 4/36 objects can be classified as a type 1 AGN, meaning that most objects in our DOG sample are type 2 AGNs (see Table 1). One prominent feature in these spectra is that they often show broad asymmetric profiles of [O III] lines, which could indicate some IR-bright DOGs are blowing out ionized gas. In order to characterize this [O III] outflow quantitatively, we need to perform a detailed spectral fitting for each spectrum. Since most objects in our sample are type 2 AGNs, the stellar continuum can be seen, which enables us to measure systemic velocity determined by stellar fitting and to estimate velocity offset with respect to the systemic velocity (see Section 3.1).

Therefore, we conducted the spectral analysis for 36 IR-bright DOGs to quantify the [O III] outflow, in the same manner as Bae & Woo (2014) (see also references therein). First, we subtracted the stellar continuum by using the templates of simple stellar population models (MILES; Sánchez-Blázquez et al. 2006), and we measured the velocity of the luminosity-weighted stellar component of the host galaxy (systemic velocity) based on the best-fit model. The fitting is

based on the Penalized Pixel-Fitting method (pPXF; Cappellari & Emsellem 2004). The typical error of the measured systemic velocity is 52.6 km s^{-1} . For the starlight-subtracted spectra, we fitted the $H\beta$ and [O III] doublet ([O III] $\lambda 4959, 5007$) with a single- and double-Gaussian function separately using MPFIT, an IDL χ^2 -minimization routine (Markwardt et al. 2009). We assume that the $H\beta$ and [O III] doublet have independent kinematics, while the [O III] lines (4959\AA and 5007\AA) have the same velocity and velocity dispersion to each other. If the peak amplitude of broad component between the two Gaussian profiles is larger than the continuum noise (i.e., the amplitude-to-noise ratio is larger than 2), we adopted the fitting results with a double-Gaussian function. Otherwise, we adopted the result with a single Gaussian. Note that we visually checked whether the stellar continuum is reproduced well by the best-fit stellar fitting. We confirmed that 10/36 objects are well-fitted by the stellar template. For the remaining 26 objects, we alternatively utilized the narrow component of the $H\beta$ line as a proxy of the systemic velocity.

3. RESULTS

3.1. Spectral fitting

Using the best fit with single- or double- Gaussian components, we measured the velocity offset (v_{line}) and velocity dispersion (σ_{line}) in the same manner as Woo et al. (2016);

$$v_{\text{line}}(\lambda) = \frac{(\lambda_0 - \lambda_{\text{rest}})c}{\lambda_{\text{rest}}} - v_{\text{sys}}(\lambda), \quad (1)$$

$$\sigma_{\text{line}}(\lambda) = \sqrt{\frac{\int \lambda^2 f(\lambda) d\lambda}{\int f(\lambda) d\lambda} - \lambda_0^2}, \quad (2)$$

where λ_{rest} is the rest-frame line center of a line ($\lambda_{\text{rest}} = 5008.24 \text{\AA}$ for [O III]), and c is the speed of light,

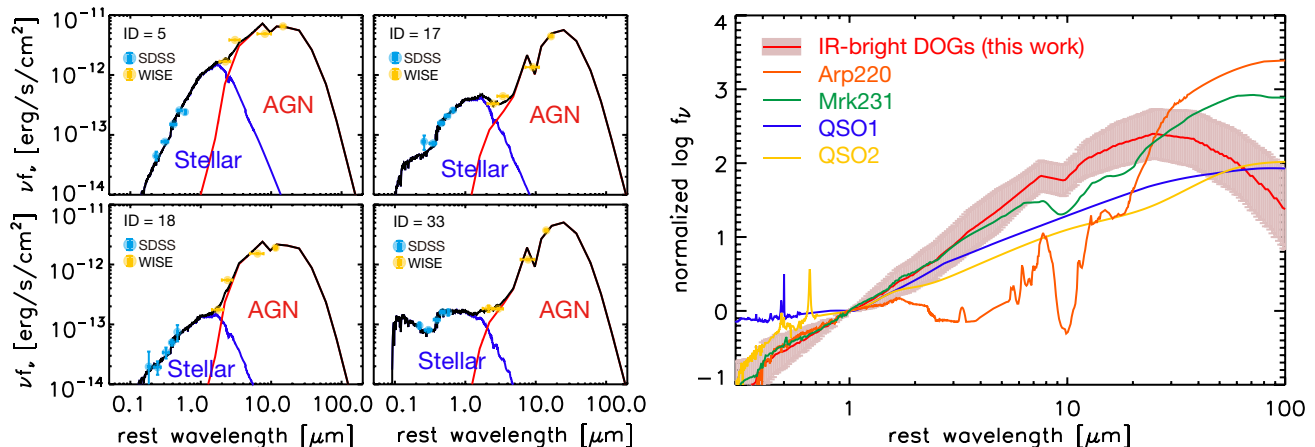


Figure 3. (Left) Examples of the SED fitting for the IR-bright DOG sample. The cyan and yellow circles represent the data from the SDSS and WISE, respectively. The contribution from the stellar and AGN components to the total SEDs are shown in blue and red lines, respectively. The black solid line represents the resultant (the combination of the stellar and AGN) SEDs. (Right) Comparison of composite spectrum of IR-bright DOGs (red line with shaded region) with other SED templates of local ULIRGs/AGNs presented by Polletta et al. (2007). Each SED is normalized by the flux density at 1 μm .

while $v_{\text{sys}}(\lambda)$ is the systemic velocity measured by the fitting with a stellar component or a narrow component of $\text{H}\beta$ (see Section 2). $f(\lambda)$ is the flux density at each wavelength and λ_0 is the first moment of the line profile (flux-weighted center),

$$\lambda_0 = \frac{\int \lambda f(\lambda) d\lambda}{\int f(\lambda) d\lambda}. \quad (3)$$

The measured velocity dispersions were corrected for the wavelength-dependent instrumental resolution of the SDSS. The measurement errors were estimated from a Monte Carlo realization; we adopted 1σ dispersion of each value by measuring them 100 times for spectra with randomly adding the noise (see Woo et al. 2016, in detail).

The resultant velocity offset ($v_{[\text{OIII}]}$) and dispersion ($\sigma_{[\text{OIII}]}$) for $[\text{OIII}]$ line of our DOG sample are tabulated in Table 1. We found that 29/36 objects show a broad wing of $[\text{OIII}]$ (we labeled them as $w_{[\text{OIII}]} = 1$; see Table 1), and thus we fit them with double Gaussian. For the remaining 7 objects ($w_{[\text{OIII}]} = 0$), we fit them with single Gaussian. Figure 2 shows some examples of the SDSS composite images made by g , r , and i images. Some DOGs show a green or red color since strong $[\text{OIII}]$ line fall in the r - or i -band, depending on the redshift.

Hereafter we compare outflow properties of our IR-bright DOG sample with those of local Seyfert 2 galaxies (Sy2s). In order to ensure a fair comparison, we only focus on $36 - 4 = 32$ IR-bright DOGs that are classified as type 2 AGNs unless otherwise noted. Note that among 32 DOGs, 12 objects have very large uncertainties of velocity offset ($\delta_{v_{[\text{OIII}]}}$), i.e., $\delta_{v_{[\text{OIII}]}} > v_{[\text{OIII}]}$ although all objects have $\delta_{\sigma_{[\text{OIII}]}} < \sigma_{[\text{OIII}]}$. We exclude them

and focus on $32 - 12 = 20$ DOGs when arguing about the velocity offset. We found that 24/32 ($\sim 75\%$) IR-bright DOGs have a large ($> 300 \text{ km s}^{-1}$) velocity dispersion, which is larger than that of local Sy2s at $z < 0.3$ (Woo et al. 2016) who reported that only 3.58% of Sy2 sample show $\sigma_{[\text{OIII}]} > 300 \text{ km s}^{-1}$. Also, 19/20 ($\sim 95\%$) DOGs have $|v_{[\text{OIII}]}| > 50 \text{ km s}^{-1}$, that is larger than those ($\sim 50\%$) of local (narrow line) Seyfert 1 and 2 galaxies (e.g., Komossa et al. 2008; Zhang et al. 2011; Bae & Woo 2014). Since the velocity offset and (particularly) velocity dispersion is expected to be due to the ionized gas outflow, this large outflow fraction could indicate that IR-bright DOGs are likely to be a good laboratory to investigate AGN feedback phenomenon (see also Section 3.3).

3.2. Relation between $[\text{OIII}]$ luminosity and IR luminosity

Here we estimated the extinction-corrected $[\text{OIII}]$ luminosity using the following formula (see Calzetti et al. 1994; Domínguez et al. 2013);

$$L_{[\text{OIII}]}^{\text{cor}} = L_{[\text{OIII}]}^{\text{obs}} 10^{0.4k_{[\text{OIII}]} E(B-V)}, \quad (4)$$

where $L_{[\text{OIII}]}^{\text{obs}}$ is the observed $[\text{OIII}]$ luminosity, $k_{[\text{OIII}]}$ is the extinction value at $\lambda = 5008.24 \text{ \AA}$ provided by Calzetti et al. (2000), and $E(B-V)$ is the color excess. We note that $E(B-V)$ was estimated based on the spectral energy distribution (SED) fitting with a code; SED Analysis using Bayesian Statistics (SEABAS; Rovilos et al. 2014). This fitting code provides up to three-component fitting (AGN, SF, and stellar component) based on the maximum likelihood method (see Rovilos et al. 2014; Toba & Nagao 2016, in detail). Among three components fitting, $E(B-V)$ was determined by the stellar component fitting with a library

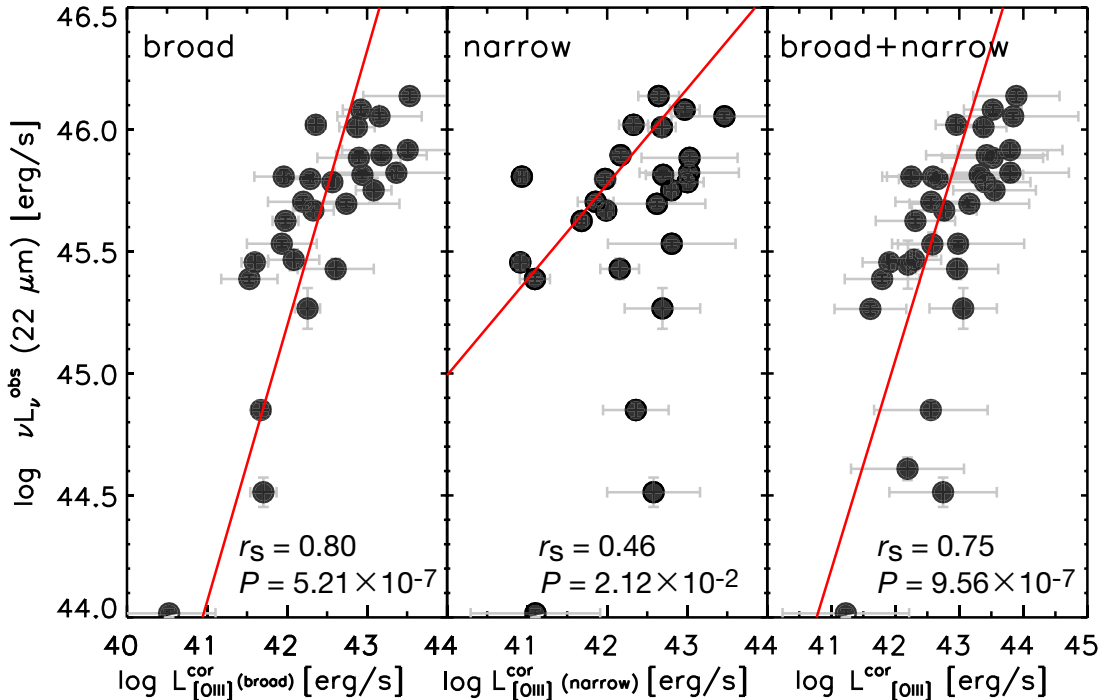


Figure 4. The $22\ \mu\text{m}$ luminosity at observed frame as a function of [O III] luminosity of broad component (left), [O III] luminosity of narrow component (middle), and [O III] luminosity (right). The red line shows the best-fit linear function. The Spearman rank correlation coefficients (r_s) with null hypothesis probabilities (P) for each relation are noted at the bottom right of each panel.

of synthetic stellar templates from [Bruzual & Charlot \(2003\)](#) stellar population models reddened using a [Calzetti et al. \(2000\)](#) dust extinction law. We used 9 photometric data (u , g , r , i , and z , and 3.4, 4.6, 12, and $22\ \mu\text{m}$, obtained from the SDSS and *WISE*, respectively) for the SED fitting. We note that all DOGs in our sample were detected in all 9 bands. The typical value of $E(B-V)$ is 0.70. We also calculated the $22\ \mu\text{m}$ luminosity at the observed frame, $\nu L_\nu^{\text{obs}}(22\ \mu\text{m})$, from the observed flux multiplied by $4\pi d_L^2$ for each DOG, where d_L is the luminosity distance. IR-bright DOGs tend to have flat SED at the MIR regime (see [Toba & Nagao 2016](#); [Toba et al. 2017b](#)) and we found that $\nu L_\nu^{\text{obs}}(22\ \mu\text{m})$ is perfectly correlated with IR luminosity ([Toba et al. 2017b](#)). In addition, some authors claimed that IR luminosity of AGNs are correlated with [O III] luminosity (e.g., [Goto et al. 2011](#)), suggesting that $22\ \mu\text{m}$ luminosity at observed frame correlates with [O III] luminosity.

Figure 3 shows examples of the SED fitting in which the data are well-fitted by SEABASSs (see also [Toba & Nagao 2016](#)). Their composite spectrum normalized by the flux density at $1\ \mu\text{m}$ is also shown in this Figure. Some SED templates of local ULIRGs and AGNs presented by [Polletta et al. \(2007\)](#) are also plotted. Compared with these templates, our IR-bright DOG sample shows a steep SED in the near-IR (NIR) and MIR regions that could be originated from hot dust heated by strong AGN radiations.

Figure 4 shows the relation between [O III] luminosity and $22\ \mu\text{m}$ luminosity at observed-frame. As many authors have reported that [O III] luminosity are well-correlated with MIR luminosity (e.g., [Toba et al. 2014](#); [Yuan et al. 2016](#); [Sun et al. 2017](#)) for SDSS galaxies/AGNs, we confirmed that [O III] luminosity correlates with $22\ \mu\text{m}$ (but at observed-frame) luminosity for our DOG sample, which is useful to infer the expected [O III] luminosity for IR-bright DOG from $22\ \mu\text{m}$ flux density without considering the k -correction. The relations between the [O III] luminosity for each of the broad and narrow component and $\nu L_\nu^{\text{obs}}(22\ \mu\text{m})$ are also shown in Figure 4. Note that if an object does not have broad [O III] wing (see Section 2), we derive extinction corrected [O III] luminosity based on result with single Gaussian fitting, and use them as $L_{[\text{OIII}]}^{\text{cor}}$ (broad+narrow). In other words, [O III] luminosity of broad and narrow component in left and middle panel of Figure 4 are derived only from objects with broad wing. We fitted each relation with linear regression lines using a IDL routine, MPFITEXY, that takes into account errors in both variables. The Spearman rank correlation coefficients (r_s) for $L_{[\text{OIII}]}^{\text{cor}}$ (broad) $-\nu L_\nu^{\text{obs}}(22\ \mu\text{m})$, $L_{[\text{OIII}]}^{\text{cor}}$ (narrow) $-\nu L_\nu^{\text{obs}}(22\ \mu\text{m})$, and $L_{[\text{OIII}]}^{\text{cor}}$ (broad+narrow) $-\nu L_\nu^{\text{obs}}(22\ \mu\text{m})$ relations are ~ 0.80 , 0.46 , and 0.75 with null hypothesis probabilities $P \sim 5.21 \times 10^{-7}$, 2.12×10^{-2} , and 9.56×10^{-7} , respectively. This means that $\nu L_\nu^{\text{obs}}(22\ \mu\text{m})$ is well-correlated with broad com-

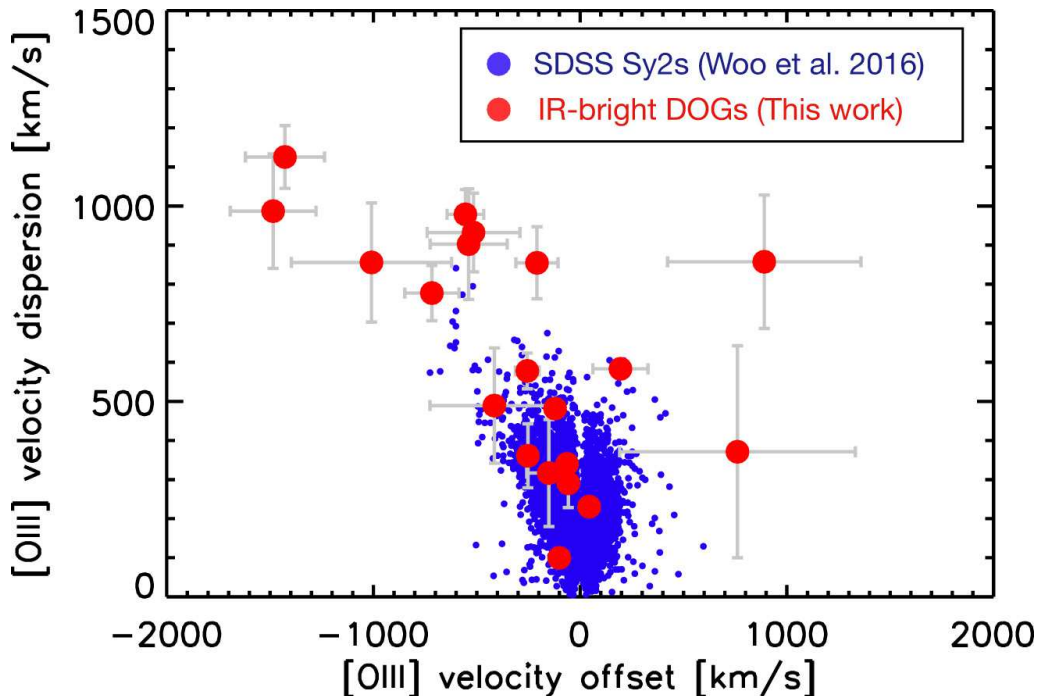


Figure 5. [O III] velocity offset – velocity dispersion (VVD) diagram for IR-bright DOGs (red circle) and SDSS Seyfert 2 galaxies (blue circle) derived by Woo et al. (2016).

ponent of [O III] luminosity. Note that the SEDs of our IR-bright DOG sample at around $22 \mu\text{m}$ appears flat as shown in Figure 3 (see also Toba et al. 2017b). Given the somewhat narrow redshift range of our sample ($0.05 < z < 1.02$), the luminosity in the MIR regime is roughly constant, which would result in a correlation even when using the observed-frame $22 \mu\text{m}$ luminosity. Since $22 \mu\text{m}$ luminosity could trace AGN activity and the broad component is likely to be more strongly affected by AGN outflows compared to the narrow component, broad component of [O III] outflow tends to have better correlation with $22 \mu\text{m}$ luminosity. We should keep in mind that, at the same time, the above correlation may be applicable only for IR-bright DOGs because whether or not other population follows this relation is still unknown.

3.3. VVD diagram

Here we show the [O III] velocity offset with respect to the systemic velocity and velocity dispersion diagram (hereafter VVD diagram) for our IR-bright DOG sample and the SDSS Seyfert 2 galaxy sample taken from Woo et al. (2016), who investigated outflow properties using a large sample of $\sim 40,000$ Sy2s at $z < 0.3$. Figure 5 shows the resultant VVD diagram of IR-bright DOGs and SDSS Sy2s where objects only with $\delta_{V_{[\text{OIII}]}} < V_{[\text{OIII}]}$ and $\delta_{\sigma_{[\text{OIII}]}} < \sigma_{[\text{OIII}]}$ are plotted. We found that 16/20 (80%) DOGs show blueshifted [O III], which supports the biconical outflow model combined with dust extinction suggested by

Crenshaw et al. (2010) (see also Barrows et al. 2013); the redshifted component of outflow (receding cone) tends to be easily hidden by foreground dust. However, this fraction (0.80) is larger than that of SDSS Sy2s (0.56) with $v_{[\text{OIII}]}$ measurements better than 1σ probably because receding component of outflowing gas in DOGs is more preferentially hidden by large amount of dust. Although the dust geometry between DOGs and Sy2s could be different, it is easy for DOGs to hide the receding outflow than approaching outflows to the line-of-sight. We also found that the majority of the IR-bright DOGs lie above the SDSS Sy2 on the VVD diagram. These results could indicate that the IR-bright DOGs are associated with stronger ionized gas outflow (but see Section 4.1).

4. DISCUSSIONS

4.1. VVD diagram as a function of IR luminosity

In Section 3.3, we found the IR-bright DOG sample has larger velocity offset and dispersion than those of SDSS Sy2 sample on the VVD diagram. However, one caution is that more luminous AGN could drive stronger outflow, i.e., we have to compare outflow properties with fixed AGN luminosity. Since Toba & Nagao (2016) derived IR luminosity contributed from AGN, $L_{\text{IR}}(\text{AGN})$, using the SED fitting for IR-bright DOG sample, we estimated the $L_{\text{IR}}(\text{AGN})$ also for the SDSS Sy2 sample. In order to derive precise IR luminosity contributed from AGN, we compiled far-IR (FIR) data

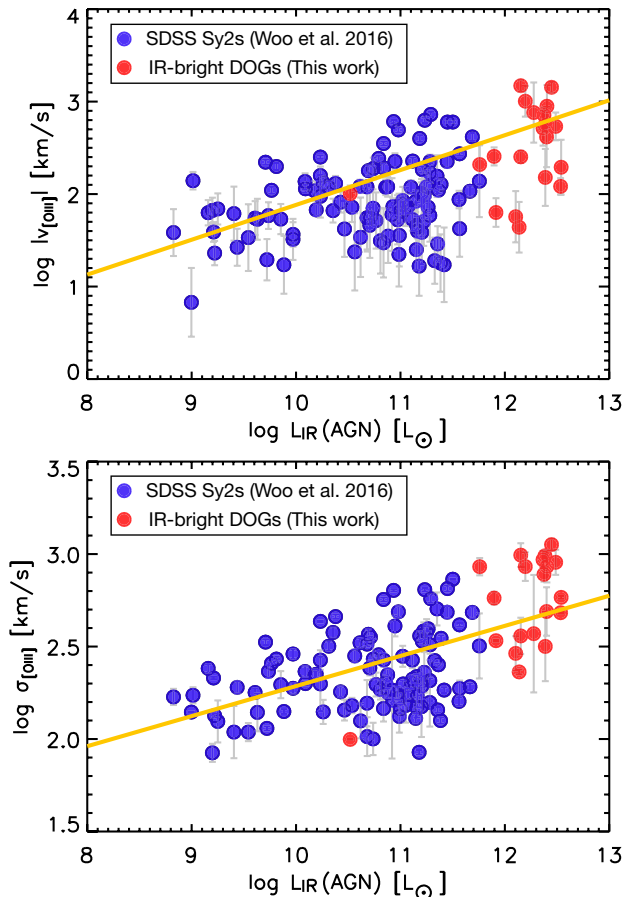


Figure 6. The absolute value of the velocity offset (top) and dispersion (bottom) as a function of IR luminosity contributed from AGN for IR-bright DOG sample (red) and SDSS Sy2 sample (blue). The yellow lines represent the best-fit linear function for both data.

using *AKARI* (Murakami et al. 2007) Far-Infrared Surveyor (FIS: Kawada et al. 2007) bright source catalogue (BSC) version 2.0 (I. Yamamura et al. in preparation). We selected about 400 objects with 65, 90, 140, and 160 μm data from SDSS Sy2 sample in Woo et al. (2016), and conducted the SED fitting with SEABASS in the same manner as Toba et al. (2017b). Note that we confirmed that the resultant IR luminosity based on this method is consistent with those in local SDSS galaxies selected from Salim et al. (2016) (see Toba et al. 2017b, in detail).

Figure 6 shows the absolute value of the velocity offset and velocity dispersion as a function of IR luminosity contributed from AGNs for IR-bright DOGs and SDSS Sy2s. We found that they are continuously distributed on those planes, and $L_{\text{IR}}(\text{AGN})$ is well-correlated both with velocity offset and dispersion. We obtained the following correlation formulae:

$$\begin{aligned} \log |v_{[\text{OIII}]}| &= (0.377 \pm 0.002) \log L_{\text{IR}}(\text{AGN}) \\ &\quad - (1.887 \pm 0.024), \\ \log \sigma_{[\text{OIII}]} &= (0.163 \pm 0.001) \log L_{\text{IR}}(\text{AGN}) \end{aligned} \quad (5)$$

$$+ (0.660 \pm 0.012). \quad (6)$$

Also, our IR-bright DOG sample is basically brighter than Sy2 galaxies, which means that the offset of IR-bright DOG sample compared to SDSS Sy2 sample on the VVD diagram shown in Figure 5 is likely due to the difference of IR luminosity originating from AGN activity.

It should be noted that the velocity offset or velocity dispersion itself is not always a good indicator of the strength of AGN outflows because they are affected by dust extinction (Bae & Woo 2016). However, the influence of dust extinction can be minimized if we use the following quantity (Bae & Woo 2016; Bae et al. 2017);

$$\sigma_0 = \sqrt{v_{[\text{OIII}]}^2 + \sigma_{[\text{OIII}]}^2}. \quad (7)$$

Figure 7 shows the relation between σ_0 and AGN luminosity. They are well correlated with each other and we obtained the following correlation formula:

$$\log \sigma_0 = (0.241 \pm 0.001) \log L_{\text{IR}}(\text{AGN}) - (0.152 \pm 0.011). \quad (8)$$

The Spearman rank correlation coefficients (r_s) for $L_{\text{IR}}(\text{AGN}) - v_{[\text{OIII}]}$, $L_{\text{IR}}(\text{AGN}) - \sigma_{[\text{OIII}]}$, and $L_{\text{IR}}(\text{AGN}) - \sigma_0$ are ~ 0.51 , 0.51 , and 0.54 with null hypothesis probabilities $P \sim 7.04 \times 10^{-10}$, 4.88×10^{-10} , and 6.10×10^{-11} , respectively. We confirmed that the correlation between σ_0 and $L_{\text{IR}}(\text{AGN})$ is slightly stronger than that of others. Note that Woo et al. (2016) reported that σ_0 of SDSS Sy2s correlates with $[\text{O III}]$ luminosity where they used $[\text{O III}]$ luminosity as an indicator of AGN luminosity. We conclude that more luminous AGN traced by $L_{\text{IR}}(\text{AGN})$ or $L_{[\text{OIII}]}$ drives strong outflows. Wagner & Bicknell (2011) conducted hydrodynamical simulations of AGN feedback in gas-rich galaxies and concluded that outflow velocities and dispersions of energy driven outflows are determined by the power of the AGN, and all the scatter is determined by the properties of the interstellar medium (ISM) properties, in particular the column density of clumpy gas (see also Wagner et al. 2013). Bieri et al. (2017) showed with radiation hydrodynamic simulations of AGN outflows that, for radiation driven winds, the infrared photons provide most of the mechanical advantage to drive outflows to high velocities, and that the properties of the outflows evolved according to the optical depth of infrared photons. Our observational results support the above conclusions.

4.2. σ_0 as a function of other properties

In Section 4.1, we found that σ_0 , an indicator of the strength of an AGN outflow, depends on $L_{\text{IR}}(\text{AGN})$. Here we investigate the dependence of σ_0 on other physical quantities; the black hole mass (M_{BH}), Eddington lu-

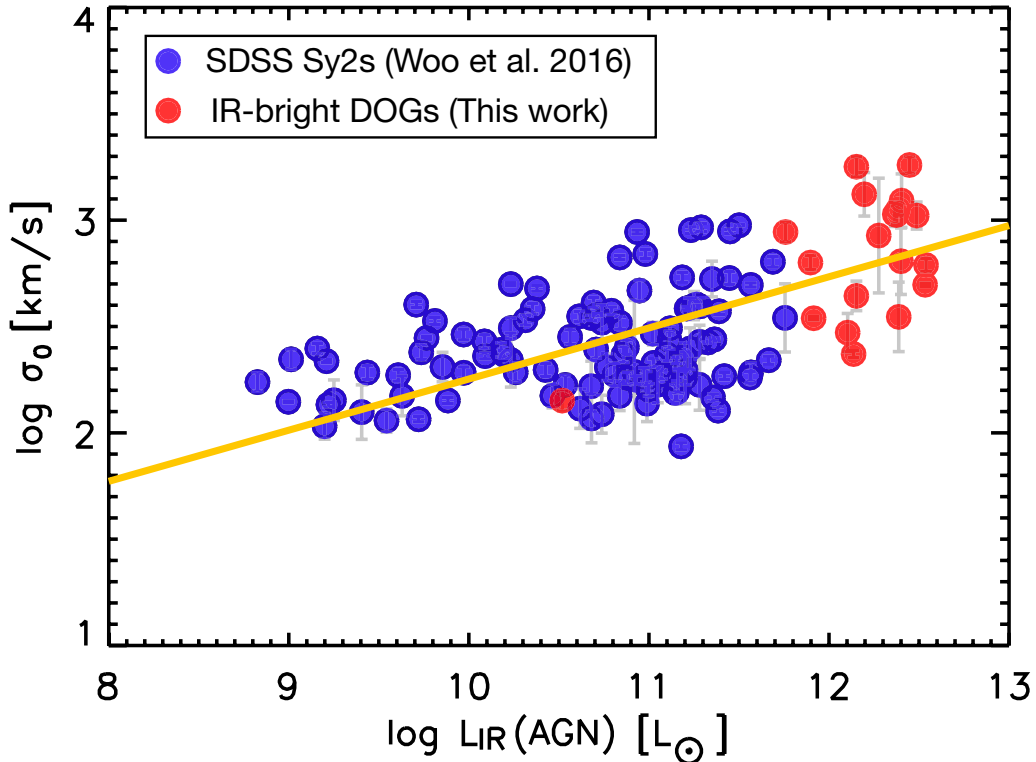


Figure 7. σ_0 as a function of IR luminosity contributed from AGN for IR-bright DOG sample (red) and SDSS Sy2 sample (blue). The yellow lines represent the best-fit linear function for both data.

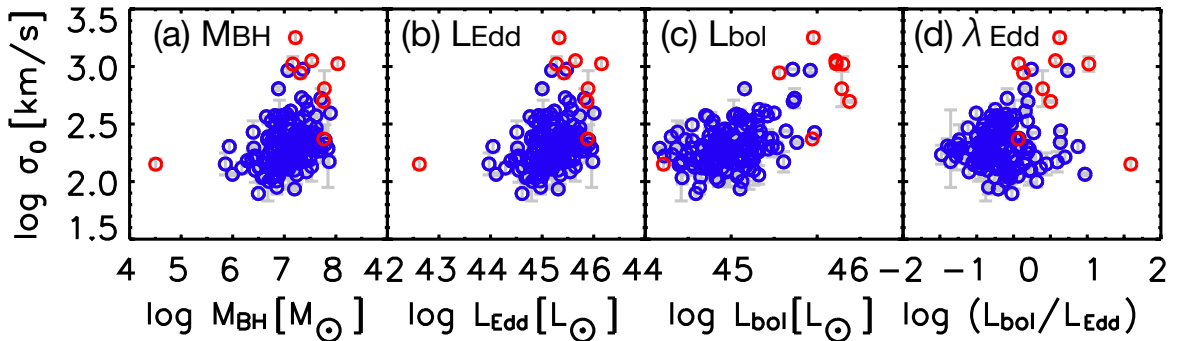


Figure 8. σ_0 as functions of (a) black hole mass, (b) Eddington luminosity, (c) bolometric luminosity, and (d) Eddington ratio. Symbols are the same as those in Figure 7.

minosity (L_{Edd}), bolometric luminosity (L_{bol}), and Eddington ratio ($\lambda_{\text{Edd}} \equiv L_{\text{bol}}/L_{\text{Edd}}$). The black hole mass is estimated from the stellar mass (M_*) by using an empirical relation reported in Reines & Volonteri (2015); $\log(M_{\text{BH}}/M_{\odot}) = 1.05 \log(M_*/10^{11}M_{\odot}) + 7.45$ with a scatter of 0.24 dex. The stellar mass is estimated using SEABASs in which we employed synthetic stellar templates from Bruzual & Charlot (2003) stellar population models assuming a Chabrier (2003) initial mass function (IMF), and reddening using a Calzetti et al. (2000) dust extinction law (see also Toba et al. 2017b). The Eddington luminosity in units of erg s^{-1} is estimated using $L_{\text{Edd}} = 1.3 \times 10^{46} (M_{\text{BH}}/10^8 M_{\odot})$ (Ferrarese & Ford 2005). The bolometric luminosity is

estimated by integrating the best-fit SED template output by SEABASs over wavelengths longward of $\text{Ly}\alpha$ in the same manner as Assef et al. (2010). Note that the mean of $L_{\text{bol}}/L_{\text{IR}}$ for IR-bright DOG is 1.61 ± 0.27 , which is consistent with that reported in Fan et al. (2016).

Figure 8 shows σ_0 as functions of black hole mass, Eddington luminosity, bolometric luminosity, and Eddington ratio. For any of these quantities, the values of σ_0 of IR-bright DOGs tend to be larger than those of Sy2. However, the correlations of these quantities with σ_0 are not strong compared to the correlation of L_{IR} (AGN) with σ_0 . Their Spearman rank correlation coefficients are less than 0.4, which could indicate that M_{BH} ,

L_{Edd} , L_{bol} , and λ_{Edd} is unlikely to be a primal parameter while L_{IR} (AGN) is a primal parameter tracing the outflow strength.

4.3. Energetics of AGN outflows

We discuss the energetics of AGN-driven outflows in terms of the mass outflow rate, energy injection rate, and momentum flux of our IR-bright DOG sample. However, an accurate estimate of these quantities is challenging because such estimates require detailed kinematic modeling for each object. We thus adopt a simple outflow model for the entire sample to provide first order constraints on the energetics of IR-bright DOGs.

If we assume a spherical volume of outflowing ionized gas (e.g., Harrison et al. 2014; Bae et al. 2017), the mass outflow rate (\dot{M}_{out}), energy injection rate (\dot{E}_{out}), and momentum flux (\dot{P}_{out}) are given by

$$\dot{M}_{\text{out}} = \frac{3M_{\text{gas}}v_{\text{out}}}{R_{\text{out}}}, \quad (9)$$

$$\dot{E}_{\text{out}} = \frac{1}{2}\dot{M}_{\text{out}}v_{\text{out}}^2, \quad (10)$$

$$\dot{P}_{\text{out}} = \dot{M}_{\text{out}}v_{\text{out}}, \quad (11)$$

where M_{gas} is the ionized gas mass, R_{out} is the outflow radius, and v_{out} is the flux-weighted intrinsic outflow velocity or bulk velocity of the outflows. Assuming case B recombination, the mass of $\text{H}\beta$ emitting gas can be estimated as follows (Nesvadba et al. 2011):

$$M_{\text{gas}} = 2.82 \times 10^9 \left(\frac{L_{\text{H}\beta}}{10^{43} \text{ erg s}^{-1}} \right) \left(\frac{n_e}{100 \text{ cm}^{-3}} \right)^{-1}, \quad (12)$$

where $L_{\text{H}\beta}$ is $\text{H}\beta$ luminosity in units of erg s^{-1} and n_e is the electron density in units of cm^{-3} . In this work, we adopt $n_e = 100 \text{ cm}^{-3}$ as routinely assumed in similar works (e.g., Liu et al. 2013b; Brusa et al. 2015) and this value is roughly consistent with that derived from [SII] doublet in a luminous obscured quasar at $z \sim 1.5$ (Perna et al. 2015). For R_{out} , we first estimate the size of the narrow line region (R_{NLR}) by using an empirical relation between R_{NLR} and extinction-uncorrected [OIII] luminosity reported by Bae et al. (2017),

$$\log R_{\text{NLR}} = (0.41 \pm 0.02) \log L_{[\text{OIII}]} - (14.00 \pm 0.77). \quad (13)$$

We then simply choose $R_{\text{out}} = 2R_{\text{NLR}}$ (Bae et al. 2017). For v_{out} , we also use an empirical relation between v_{out} and σ_0 reported by Bae et al. (2017),

$$v_{\text{out}} = (2.0 \pm 0.5)\sigma_0. \quad (14)$$

We caution that the electron density depends on the object and v_{out} depends on the dust extinction and inclination of each object (see Greene et al. 2011; Harrison et al. 2014; Bae et al. 2017, and references therein), which means that the derived quantities under

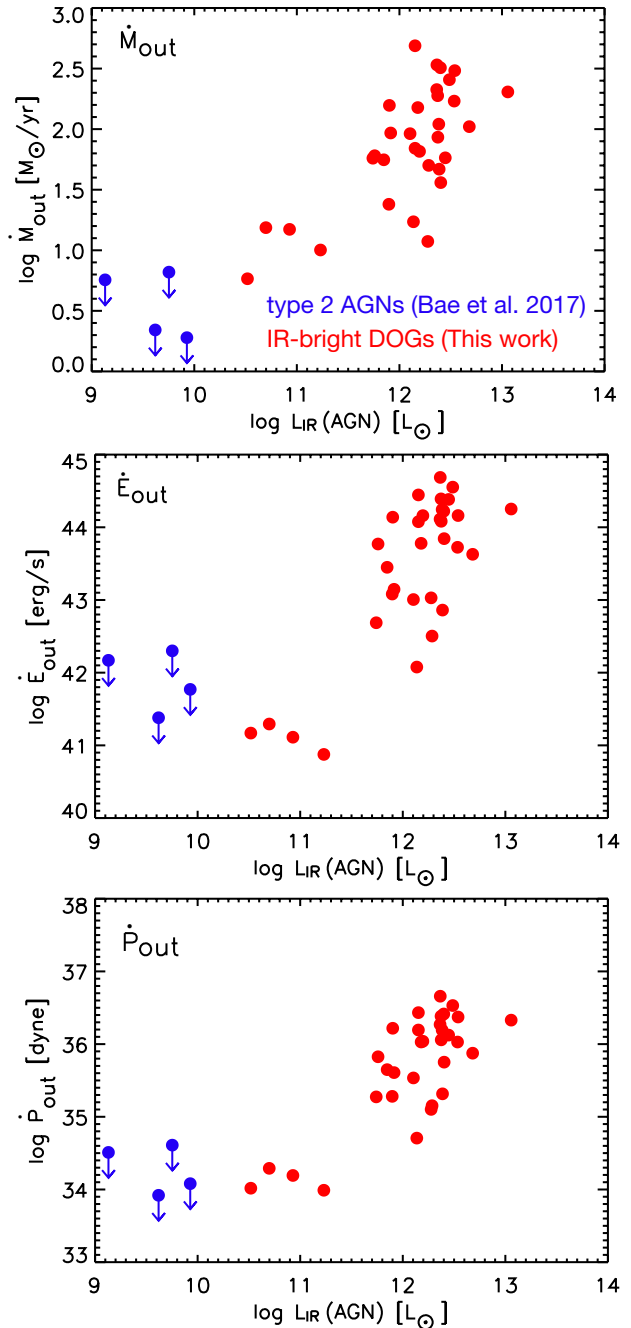


Figure 9. The mass outflow rate \dot{M}_{out} (left), the energy injection rate \dot{E}_{out} (middle), and momentum flux \dot{P}_{out} (right) as a function of IR luminosity contributed from AGNs (L_{IR} (AGN)) of IR-bright DOGs (red circle) and type 2 AGNs at $z < 0.1$ (blue circle) presented by Bae et al. (2017).

our simple assumptions could induce large uncertainties. The resultant values estimated using Equation (9)–(14) are summarized in Table 2.

Figure 9 shows the energetics (\dot{M}_{out} , \dot{E}_{out} , and \dot{P}_{out}) as a function of L_{IR} (AGN) for IR-bright DOGs and type 2 AGNs reported by Bae et al. (2017). Bae et al. (2017) observed type 2 AGNs at $z < 0.1$ with integral-field spectroscopy and investigated the energetics of

Table 2. Energetics of WISE-SDSS spec DOGs.

ID	$\log L_{\text{H}\beta}$ erg s ⁻¹	$\log M_{\text{gas}}$ M_{\odot}	$\log v_{\text{out}}$ km s ⁻¹	$\log R_{\text{out}}$ pc	$\log \dot{M}_{\text{out}}$ $M_{\odot} \text{ yr}^{-1}$	$\log \dot{E}_{\text{out}}$ erg s ⁻¹	$\log \dot{P}_{\text{out}}$ dyne	$\frac{\dot{P}_{\text{out}}}{L_{\text{IR}}(\text{AGN})/c}$
1	41.7	8.2	2.3	3.8	1.2	41.3	34.3	3.0
2	41.3	7.8	3.6	4.1	1.8	44.4	36.1	3.7
3	41.4	7.9	2.8	3.5	1.7	42.9	35.3	0.7
4	41.2	7.7	2.7	3.6	1.2	42.1	34.7	0.3
5	41.7	8.1	3.4	3.9	2.0	44.2	36.2	5.0
6	41.3	7.8	3.3	3.7	1.9	44.1	36.1	3.8
7	41.7	8.2	3.2	3.7	2.2	44.1	36.2	16.1
8	42.9	9.4	2.9	4.1	2.7	44.1	36.4	14.9
9	42.2	8.7	2.8	3.9	2.0	43.0	35.5	2.1
10	42.0	8.5	3.1	4.0	2.0	43.6	35.9	1.2
11	41.5	7.9	2.2	3.6	1.0	40.9	34.0	0.4
14	41.1	7.6	3.6	3.7	1.8	44.4	36.2	8.6
15	42.4	8.8	3.1	3.9	2.5	44.2	36.4	8.1
16	40.5	6.9	3.2	3.6	1.1	43.0	35.1	0.5
17	40.6	7.1	3.1	3.3	1.4	43.1	35.3	1.9
18	42.6	9.1	3.1	4.2	2.5	44.2	36.4	5.3
19	42.3	8.8	3.1	4.1	2.3	44.1	36.3	6.3
20	42.4	8.9	3.2	4.3	2.3	44.3	36.3	1.5
21	41.6	8.0	3.1	3.9	1.7	43.4	35.6	4.9
23	41.8	8.2	2.2	3.7	1.2	41.1	34.2	1.4
24	42.1	8.5	3.3	4.0	2.3	44.4	36.4	8.0
25	41.6	8.0	2.7	3.5	1.7	42.5	35.2	0.6
27	42.2	8.6	2.8	4.0	2.0	43.1	35.6	3.8
28	41.0	7.5	3.2	3.4	1.8	43.8	35.8	9.1
29	42.4	8.9	3.0	4.1	2.2	43.7	36.0	2.4
30	42.2	8.7	3.3	4.1	2.4	44.6	36.5	8.6
31	42.4	8.8	3.1	4.2	2.2	43.8	36.0	5.5
32	41.3	7.7	3.4	3.8	1.8	44.2	36.0	5.4
33	42.0	8.5	3.3	3.7	2.5	44.7	36.7	15.3
34	42.0	8.4	2.7	3.9	1.8	42.7	35.3	2.7
35	40.8	7.3	3.4	3.6	1.6	43.8	35.8	1.7
36	40.6	7.0	2.5	3.2	0.8	41.2	34.0	2.5

them. We estimate their $L_{\text{IR}}(\text{AGN})$ based on the SED fitting in the same manner as those we described in Section 4.1 and 4 AGNs are plotted in Figure 9. We found that our IR-bright DOG sample have systematically larger values than those of local type 2 AGNs. Since these values are clearly connected to AGN activity as shown in Figure 9 (see also Bae et al. 2017), this result can be explained by the difference of AGN luminosity as discussed in Section 4.1.

We also estimate the “momentum boost”, i.e., the ratio of the momentum flux (\dot{P}) and the AGN radiative momentum output ($L_{\text{IR}}(\text{AGN})/c$) (see Table 2). We found that the estimated initial velocity (v_{in}) from nucleus for most objects assuming that the observed outflows are energy-conserving (see Faucher-Giguère & Quataert 2012; Ciccone et al. 2014)

is $v_{\text{in}} = (0.01 - 0.2)c$. This result suggests that some IR-bright DOGs show an ultrafast outflow (UFO) with $v_{\text{in}} = (0.05 - 0.3)c$ (e.g., Tombesi et al. 2011; Gofford et al. 2013).

4.4. VVD diagram for other lines

We discuss the outflow properties of other emission lines. Figure 10 shows examples of the spectra fitting for [O II] λ 3727 and [Ne III] λ 3869 lines. Both lines are well-fitted by single or double Gaussians.

Figure 11 show the VVD diagram for [Ne III], [O II], and [O III] for our IR-bright DOG sample. We found that [Ne III] have similar velocity offset and dispersion as those of [O III] while [O II] have smaller values than those of [O III]. It should be noted that [O II] is not well fitted with double Gaussian component in many cases

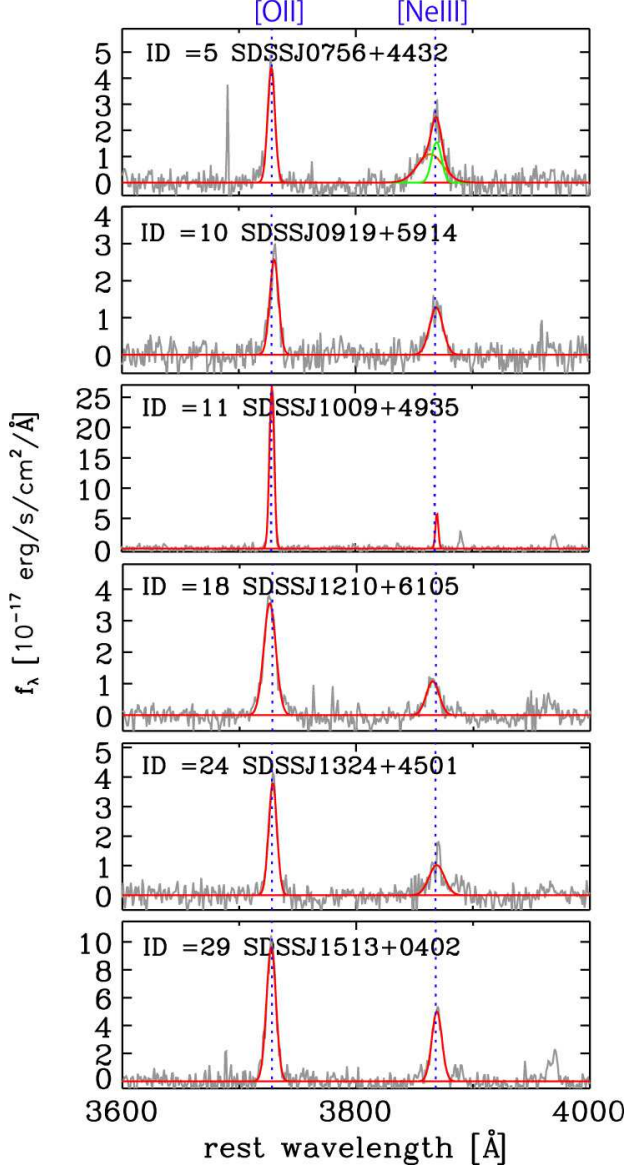


Figure 10. The example of spectral fitting for [O II] and [Ne III] lines. Gray line shows the starlight-subtracted spectra. The red line shows the best fitting with single or double Gaussian for each emission line. The green and orange lines show narrow and broad emission line component, respectively. The vertical blue dashed lines correspond to the rest-frame wavelength for [O II] and [Ne III] lines.

due to the blending of $\lambda 3726, 3729 \text{ \AA}$ doublet. If we use only a single Gaussian, alternatively, it gives a lot larger velocity dispersion ($\sigma_{[\text{O II}]}$). We should keep in mind the above uncertainties before interpreting the discrepancy between [Ne III] and [O III], and [O II] in Figure 11.

The difference of v_{line} and σ_{line} for each line tells us a hint to understand the physicochemical properties of outflowing gas. The ionization potentials of [O II] $\lambda 3727$, [O III] $\lambda 5007$, and [Ne III] $\lambda 3869$ are 13.61, 35.15, and 41.07 eV, respectively. The critical electron densities for collisional de-excitation of [O II] $\lambda 3727$, [O III] $\lambda 5007$, and

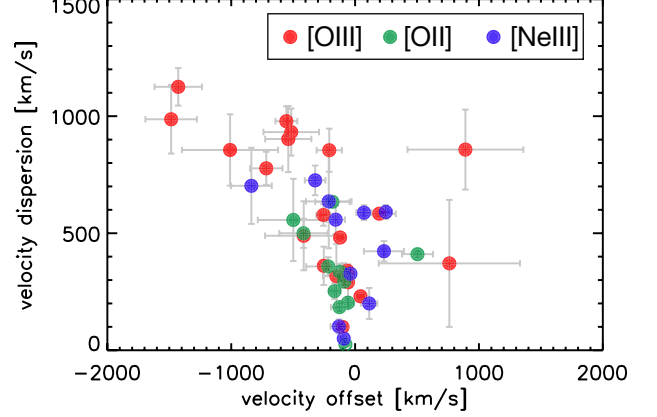


Figure 11. VVD diagram for [O II] (green), [Ne III] (blue), [O III] (red) line.

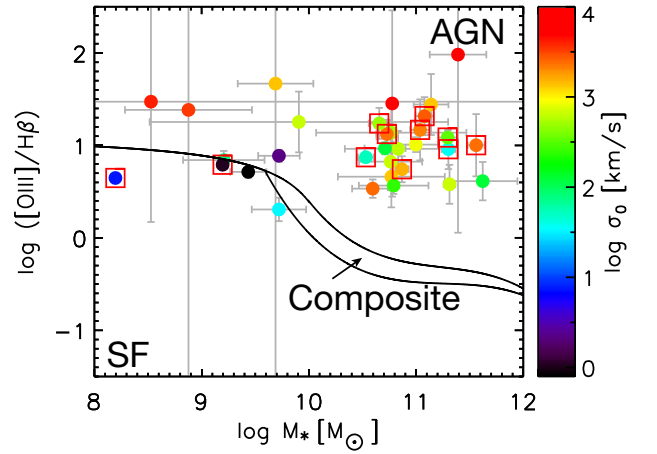


Figure 12. MEX diagnostic diagram for the IR-bright DOGs. The color scheme indicates $\sigma_0 = \sqrt{v_{[\text{O III}]}}^2 + \sigma_{[\text{O III}]}^2$. The two solid lines curves are empirically determined to distinguish AGN, SF, and composite type of galaxies. The data with red square have $\text{SN} > 3$ both for [O III]/H β and stellar mass.

[Ne III] $\lambda 3869$ are 3.4×10^3 , 6.8×10^5 , and $9.5 \times 10^6 \text{ cm}^{-3}$, respectively. The fraction of objects with $|v_{\text{line}}| > 50 \text{ km s}^{-1}$ and $\sigma_{\text{line}} > 500 \text{ km s}^{-1}$ for [O II], [O III], and [Ne III] are 0.134, 0.566, and 0.571, respectively. This means that more dense and ionized gas tend to show larger velocity offset and dispersion. Since it is naturally expected that electron densities will increase toward the nuclear region and gas located there is highly ionized by AGN radiation, [O III] and [Ne III] are ejected with high velocity while [O II] are less affected by AGN radiation, that picture is consistent with those suggested by Barrows et al. (2013) (see also Komossa et al. 2008).

4.5. MEx diagram

Finally, we discuss the Mass-Excitation (MEX) diagram (Juneau et al. 2011, 2014) that enables to perform AGN diagnostics for objects with even $z > 0.4$. Since SEABASs outputs stellar mass (M_*) and we measured [O III] and H β line flux, we here investigate where

IR-bright DOGs lie in the MEx diagram. Note that our estimate based on this method has an uncertainty because we did not take into account the influence from the scattered light by AGNs (see also Hamann et al. 2017; Toba et al. 2017b). We also note that we excluded DOGs classified as type 1 AGN (see Section 2) in this analysis because the MEx diagram is optimized for galaxies/AGNs with narrow line emission.

Figure 12 shows the MEx diagnostic diagram for the IR-bright DOGs, suggesting that IR-bright DOGs can be classified as AGNs, which is consistent from our inspection based on the SED and IR flux dependence of the AGN fraction for DOGs (see Toba et al. 2015; Toba & Nagao 2016). At the same time, there are no significant dependences of σ_0 on the MEx diagram. This could indicate that $[\text{O III}]/\text{H}\beta$ is unlikely to be a good tracer of outflow strength partly because $[\text{O III}]/\text{H}\beta$ also depends on other quantities such as metallicity. On the other hand, after removing data with large error, i.e., when focusing only on data with $\text{SN} > 3$ both for $[\text{O III}]/\text{H}\beta$ and stellar mass, stellar mass is likely to be correlated with σ_0 . Since stellar mass correlates with stellar dispersion that also correlates with σ_0 (Woo et al. 2016), this tendency is naturally expected.

5. SUMMARY

In this work, we investigated the outflowing ionized gas properties of IR-bright DOGs by performing detailed spectral analysis for their SDSS spectra. Among 67 IR-bright DOGs selected with the *WISE* and SDSS spectroscopic catalogs, 36 objects show $[\text{O III}]\lambda 5007$ line and we estimated its velocity offset with respect to the systemic velocity and velocity dispersion. In particular, we conducted spectral fitting with single or double Gaussian component depending on whether or not they have broad wing. The main results are as follows:

1. Among a sample of 32 IR-bright DOGs that are classified as type 2 AGN, 24 ($\sim 75\%$) objects have large $[\text{O III}]$ velocity dispersion with 300 km s^{-1} . This fraction is larger than other AGN populations, indicating that IR-bright DOGs show stronger ionized gas outflow.
2. The $[\text{O III}]$ luminosity is correlated with observed-frame luminosity at $22 \mu\text{m}$. In particular, the $22 \mu\text{m}$ luminosity at observed-frame may be a good indicator of the luminosity of broad component of $[\text{O III}]$ line for IR-bright DOGs.
3. The infrared luminosity contributed from AGNs for IR-bright DOG + SDSS Seyfert 2 sample is well-correlated with velocity offset ($v_{[\text{O III}]}$), dispersion ($\sigma_{[\text{O III}]}$), and particularly $\sigma_0 =$

$\sqrt{v_{[\text{O III}]}^2 + \sigma_{[\text{O III}]}^2}$. This indicates that objects with higher AGN luminosity tend to launch stronger outflowing gas.

4. IR-bright DOG sample have larger velocity offset and dispersion than those of the SDSS Seyfert 2 sample, which can be interpreted as the difference of their AGN luminosities.
5. The energetics (\dot{M}_{out} , \dot{E}_{out} , and \dot{P}_{out}) of IR-bright DOGs correlates with AGN luminosity. Some IR-bright DOGs have initial outflow velocity (v_{in}) $> 0.1c$, which means that some IR-bright DOGs show an ultrafast outflow.
6. The velocity offset and dispersion of $[\text{O III}]$ and $[\text{Ne III}]\lambda 3869$ are larger than those of $[\text{O II}]\lambda 3727$, suggesting that denser and more ionized gas are effectively affected by AGN radiation.

The authors gratefully acknowledge the anonymous referee for a careful reading of the manuscript and very helpful comments. Funding for SDSS-III has been provided by the Alfred P. Sloan Foundation, the Participating Institutions, the National Science Foundation, and the U.S. Department of Energy Office of Science. The SDSS-III web site is <http://www.sdss3.org/>. SDSS-III is managed by the Astrophysical Research Consortium for the Participating Institutions of the SDSS-III Collaboration including the University of Arizona, the Brazilian Participation Group, Brookhaven National Laboratory, Carnegie Mellon University, University of Florida, the French Participation Group, the German Participation Group, Harvard University, the Instituto de Astrofísica de Canarias, the Michigan State/Notre Dame/JINA Participation Group, Johns Hopkins University, Lawrence Berkeley National Laboratory, Max Planck Institute for Astrophysics, Max Planck Institute for Extraterrestrial Physics, New Mexico State University, New York University, Ohio State University, Pennsylvania State University, University of Portsmouth, Princeton University, the Spanish Participation Group, University of Tokyo, University of Utah, Vanderbilt University, University of Virginia, University of Washington, and Yale University. This publication makes use of data products from the Wide-field Infrared Survey Explorer, which is a joint project of the University of California, Los Angeles, and the Jet Propulsion Laboratory/California Institute of Technology, funded by the National Aeronautics and Space Administration. This research is based on observations with AKARI, a JAXA project with the participation of ESA. This research has made use of the NASA/IPAC Infrared Science

Archive, which is operated by the Jet Propulsion Laboratory, California Institute of Technology, under contract with the National Aeronautics and Space Administration. Y.Toba and W.H.Wang acknowledge the support from the Ministry of Science and Technology of

Taiwan (MOST 105-2112-M-001-029-MY3). T.Nagao is financially supported by the Japan Society for the Promotion of Science (JSPS) KAKENHI (16H01101 and 16H03958). J.H.Woo acknowledges the support by the National Research Foundation of Korea grant funded by the Korea government (No. 2016R1A2B3011457).

REFERENCES

- Alam, S., Albareti, F. D., Allende Prieto, C., et al. 2015, *ApJS*, 219, 12
- Alexander, D. M., Swinbank, A. M., Smail, I., McDermaid, R., & Nesvadba, N. P. H. 2010, *MNRAS*, 402, 2211
- Aoki, K., Kawaguchi, T., & Ohta, K. 2005, *ApJ*, 618, 601
- Assef, R. J., Kochanek, C. S., Brodwin, M., et al. 2010, *ApJ*, 713, 970
- Bae, H.-J., & Woo, J.-H. 2014, *ApJ*, 795, 30
- Bae, H.-J., & Woo, J.-H. 2016, *ApJ*, 828, 97
- Bae, H.-J., Woo, J.-H., Karouzos, M., et al. 2017, *ApJ*, 837, 91
- Barbosa, F. K. B., Storchi-Bergmann, T., Cid Fernandes, R., Winge, C., & Schmitt, H. 2009, *MNRAS*, 396, 2
- Barrows, R. S., Sandberg Lacy, C. H., Kennefick, J., et al. 2013, *ApJ*, 769, 95
- Bian, W., Yuan, Q., & Zhao, Y. 2005, *MNRAS*, 364, 187
- Bieri, R., Dubois, Y., Rosdahl, J., et al. 2017, *MNRAS*, 464, 1854
- Bischetti, M., Piconcelli, E., Vietri, G., et al. 2017, *A&A*, 598, A122
- Boroson, T. 2005, *AJ*, 130, 381
- Brusa, M., Bongiorno, A., Cresci, G., et al. 2015, *MNRAS*, 446, 2394
- Bruzual, G., & Charlot, S. 2003, *MNRAS*, 344, 1000
- Calzetti, D., Armus, L., Bohlin, R. C., Kinney, A. L., Koornneef, J., & Storchi-Bergmann, T. 2000, *ApJ*, 533, 682
- Calzetti, D., Kinney, A. L., & Storchi-Bergmann, T. 1994, *ApJ*, 429, 582
- Cano-Díaz, M., Maiolino, R., Marconi, A., Netzer, H., Shemmer, O., & Cresci, G. 2012, *A&A*, 537, L8
- Cappellari, M., & Emsellem, E. 2004, *PASP*, 116, 138
- Carniani, S., Marconi, A., Maiolino, R., et al. 2016, *A&A*, 591, A28
- Chabrier, G. 2003, *PASP*, 115, 763
- Cicone, C., Maiolino, R., Sturm, E., et al. 2014, *A&A*, 562, 21
- Crenshaw, D. M., Schmitt, H. R., Kraemer, S. B., Mushotzky, R. F., & Dunn, J. P. 2010, *ApJ*, 708, 419
- Cutri, R. M., & et al. 2014, *VizieR Online Data Catalog*, 2328, 0
- Dey, A., Soifer, B. T., Desai, V., et al. 2008, *ApJ*, 677, 943
- Di Matteo, T., Springel, V., & Hernquist, L. 2005, *Nature*, 433, 604
- Domínguez, A., Siana, B., Henry, A. L., et al. 2013, *ApJ*, 763, 145
- Fabian, A. C. 2012, *ARA&A*, 50, 455
- Fan, L., Han, Y., Nikutta, R., Drouart, G., & Knudsen, K. K. 2016, *ApJ*, 823, 107
- Faucher-Giguère, C.-A., & Quataert, E. 2012, *MNRAS*, 425, 605
- Ferrarese, L., & Ford, H. 2005, *SSRv*, 116, 523
- Gofford, J., Reeves, J. N., Tombesi, F., et al. 2013, *MNRAS*, 430, 60
- Goto, T., Arnouts, S., Malkan, M., et al. 2011, *MNRAS*, 414, 1903
- Greene, J. E., Zakamska, N. L., Ho, L. C., & Barth, A. J. 2011, *ApJ*, 732, 9
- Hamann, F., Zakamska, N. L., Ross, N., et al. 2017, *MNRAS*, 464, 3431
- Harrison, C. M., Alexander, D. M., Mullaney, J. R., & Swinbank, A. M. 2014, *MNRAS*, 441, 3306
- Hopkins, P. F., Hernquist, L., Cox, T. J., et al. 2006, *ApJS*, 163, 1
- Hopkins, P. F., Hernquist, L., Cox, T. J., & Kereš, D. 2008, *ApJS*, 175, 356
- Juneau, S., Bournaud, F., Charlot, S., et al. 2014, *ApJ*, 788, 88
- Juneau, S., Dickinson, M., Alexander, D. M., & Salim, S. 2011, *ApJ*, 736, 104
- Kawada, M., Baba, H., Barthel, P. D., et al. 2007, *PASJ*, 59, 389
- Karouzos, M., Woo, J.-H., & Bae, H.-J. 2016a, *ApJ*, 819, 148
- . 2016b, *ApJ*, 833, 171
- King, A., & Pounds, K. 2015, *ARA&A*, 53, 115
- Komossa, S., Xu, D., Zhou, H., Storchi-Bergmann, T., & Binette, L. 2008, *ApJ*, 680, 926
- Kormendy, J., & Ho, L. C. 2013, *ARA&A*, 51, 511
- Liu, G., Zakamska, N. L., Greene, J. E., Nesvadba, N. P. H., & Liu, X. 2013a, *MNRAS*, 430, 2327
- Liu, G., Zakamska, N. L., Greene, J. E., Nesvadba, N. P. H., & Liu, X. 2013b, *MNRAS*, 436, 2576
- Magorrian, J., Tremaine, S., Richstone, D., et al. 1998, *AJ*, 115, 2285
- Marconi, A., & Hunt, L. K. 2003, *ApJL*, 589, L21
- Markwardt, C. B. 2009, in *ASP Conf. Ser. 411, Astronomical Data Analysis Software and Systems XVIII*, ed. D. A. Bohlender, D. Durand, & P. Dowler (San Francisco, CA: ASP), 251
- McConnell, N. J., & Ma, C.-P. 2013, *ApJ*, 764, 184
- McElroy, R., Croom, S. M., Pracy, M., Sharp, R., Ho, I.-T., & Medling, A. M. 2015, *MNRAS*, 446, 2186
- Mullaney, J. R., Alexander, D. M., Fine, S., et al. 2013, *MNRAS*, 433, 622
- Murakami, H., Baba, H., Barthel, P., et al. 2007, *PASJ*, 59, 369
- Narayanan, D., Dey, A., Hayward, C. C., et al. 2010, *MNRAS*, 407, 1701
- Nesvadba, N. P. H., Polletta, M., Lehnert, M. D., et al. 2011, *MNRAS*, 415, 2359
- Perna, M., Brusa, M., Cresci, G., et al. 2015, *A&A*, 574, A82
- Polletta, M., Tajer, M., Maraschi, L., et al. 2007, *ApJ*, 663, 81
- Reines, A. E., & Volonteri, M. 2015, *ApJ*, 813, 82
- Rodríguez Zaurín, J., Tadhunter, C. N., Rose, M., & Holt, J. 2013, *MNRAS*, 432, 138
- Ross, N. P., Hamann, F., Zakamska, N. L., et al. 2015, *MNRAS*, 453, 3932
- Rovilos, E., Georgantopoulos, I., Akylas, A., et al. 2014, *MNRAS*, 438, 494
- Rowan-Robinson, M. 2000, *MNRAS*, 316, 885
- Salim, S., Lee, J. C., Janowiecki, S., et al. 2016, *ApJS*, 227, 2
- Sánchez-Blázquez, P., Peletier, R. F., Jiménez-Vicente, J., et al. 2006, *MNRAS*, 371, 703
- Sanders, D. B., & Mirabel, I. F. 1996, *ARA&A*, 34, 749
- Sun, A.-L., Greene, J. E., Impellizzeri, C. M. V., et al. 2013, *ApJ*, 778, 47
- Sun, A.-L., Greene, J. E., & Zakamska, N. L. 2017, *ApJ*, 835, 222
- Toba, Y., Nagao, T., Wang, W.-H., et al. 2017b, *ApJ*, 840, 21
- Toba, Y., Nagao, T., Kajisawa, M., et al. 2017a, *ApJ*, 835, 36
- Toba, Y., & Nagao, T. 2016, *ApJ*, 820, 46
- Toba, Y., Nagao, T., Strauss, M. A., et al. 2015, *PASJ*, 67, 86

- Toba, Y., Oyabu, S., Matsuhara, H., et al. 2014, *ApJ*, 788, 45
 Tombesi, F., Cappi, M., Reeves, J. N., et al. 2011, *ApJ*, 742, 44
 Villar-Martín, M., Humphrey, A., Delgado, R. G., Colina, L., & Arribas, S. 2011, *MNRAS*, 418, 2032
 Wagner, A. Y., & Bicknell, G. V. 2011, *ApJ*, 728, 29
 Wagner, A. Y., Umemura, M., & Bicknell, G. V. 2013, *ApJL*, 763, L18
 Wang, J., Mao, Y. F., & Wei, J. Y. 2011, *ApJ*, 741, 50
 Woo, J.-H., Schulze, A., Park, D., et al. 2013, *ApJ*, 772, 49
 Woo, J.-H., Bae, H.-J., Son, D., & Karouzos, M. 2016, *ApJ*, 817, 108
 Woo, J.-H., Son, D., & Bae, H.-J. 2017, *ApJ*, 839, 120
 Wright, E. L., Eisenhardt, P. R. M., Mainzer, A. K., et al. 2010, *AJ*, 140, 1868
 York, D. G., Adelman, J., Anderson, J. E., Jr., et al. 2000, *AJ*, 120, 1579
 Yuan, S., Strauss, M. A., & Zakamska, N. L. 2016, *MNRAS*, 462, 1603
 Zakamska, N. L., & Greene, J. E. 2014, *MNRAS*, 442, 784
 Zakamska, N. L., et al. 2016, *MNRAS*, 459, 3144
 Zakamska, N. L., Strauss, M. A., Krolik, J. H., et al. 2003, *AJ*, 126, 2125
 Zamanov, R., Marziani, P., Sulentic, J. W., Calvani, M., Dultzin-Hacyan, D., & Bachev, R. 2002, *ApJL*, 576, L9
 Zhang, K., Dong, X.-B., Wang, T.-G., & Gaskell, C. M. 2011, *ApJ*, 737, 71
 Zhang, S., Zhou, H., Shi, X., et al. 2017, *ApJ*, 836, 86

APPENDIX

A. THE SDSS SPECTRA OF IR-BRIGHT DOGS WITH A POWERFUL [O III] OUTFLOW

Here we present the SDSS spectra for all 36 IR-bright DOGs (Figure [A1–A4](#)).

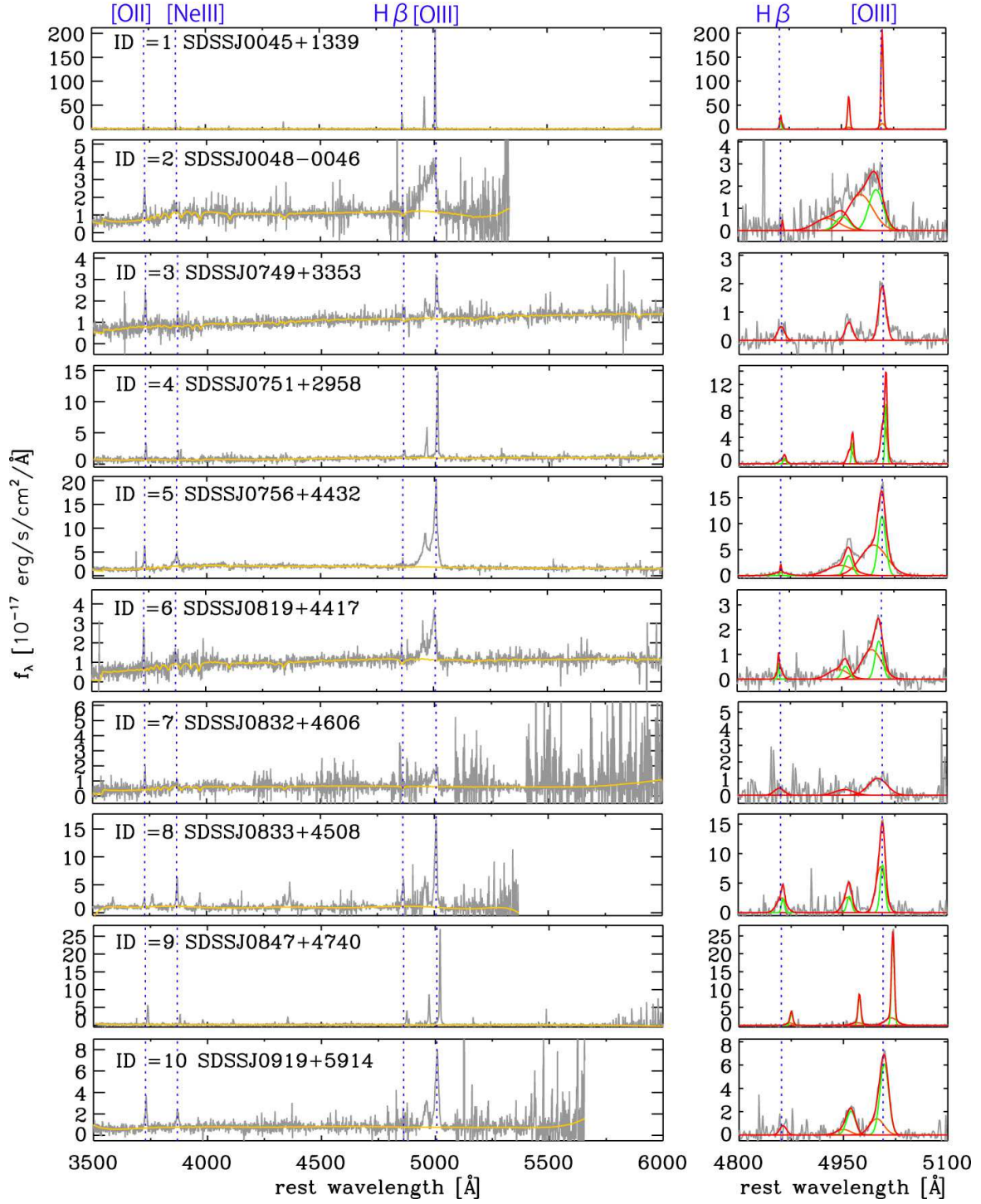


Figure A1. The SDSS spectra for IR-bright DOG sample with ID=1–10. The yellow lines show our best fits to the continuum. The right panel for each object shows the starlight-subtracted spectra with gray solid line. The red line shows the best fitting with single or double Gaussian for each emission line. The green and orange lines show narrow and broad emission line component for each double Gaussian, respectively. The vertical blue dashed lines correspond to the rest-frame wavelength for [O II], [Ne III], H β , and [O III] lines.

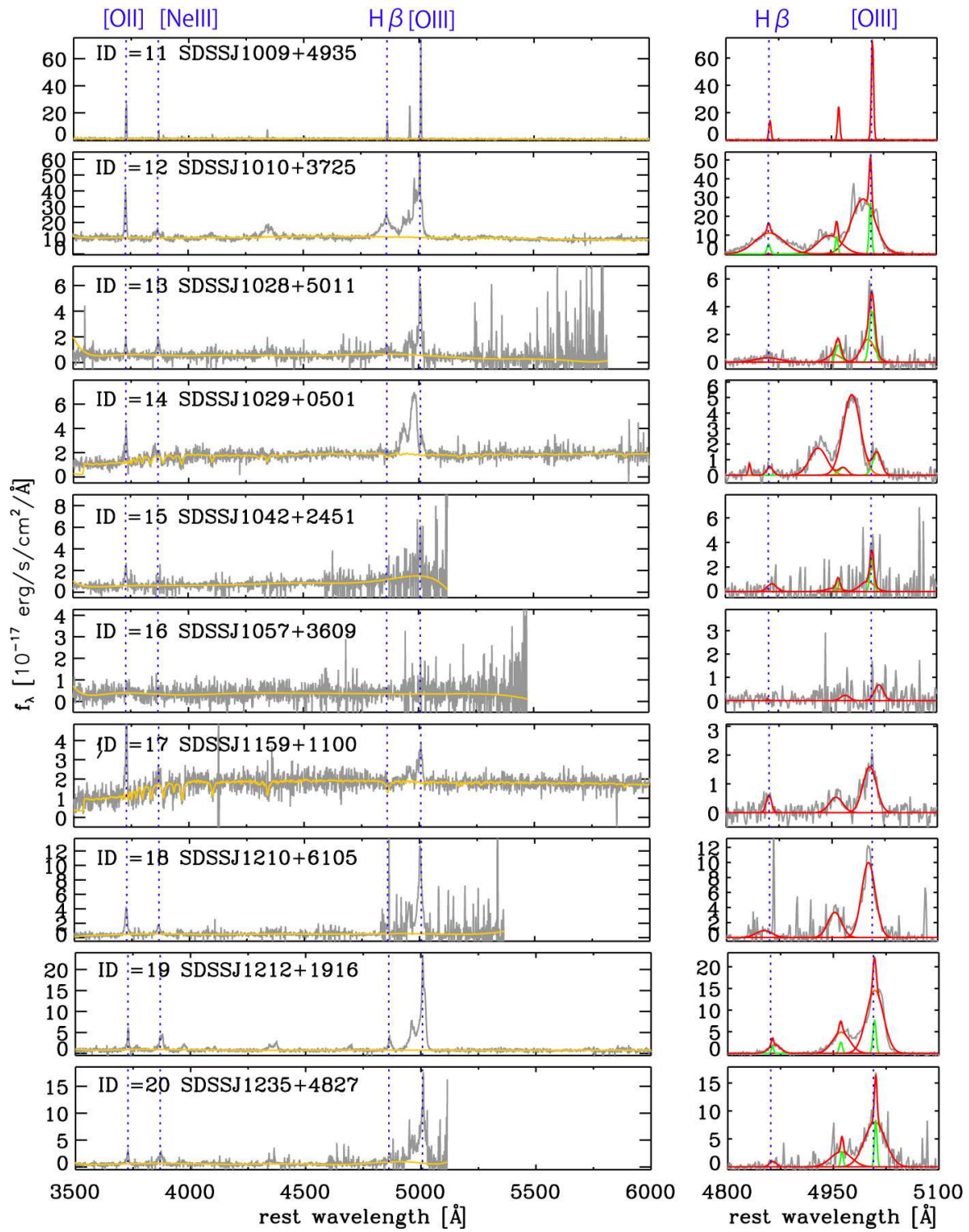


Figure A2. Same as Figure A1, but for DOGs with ID=11–20.

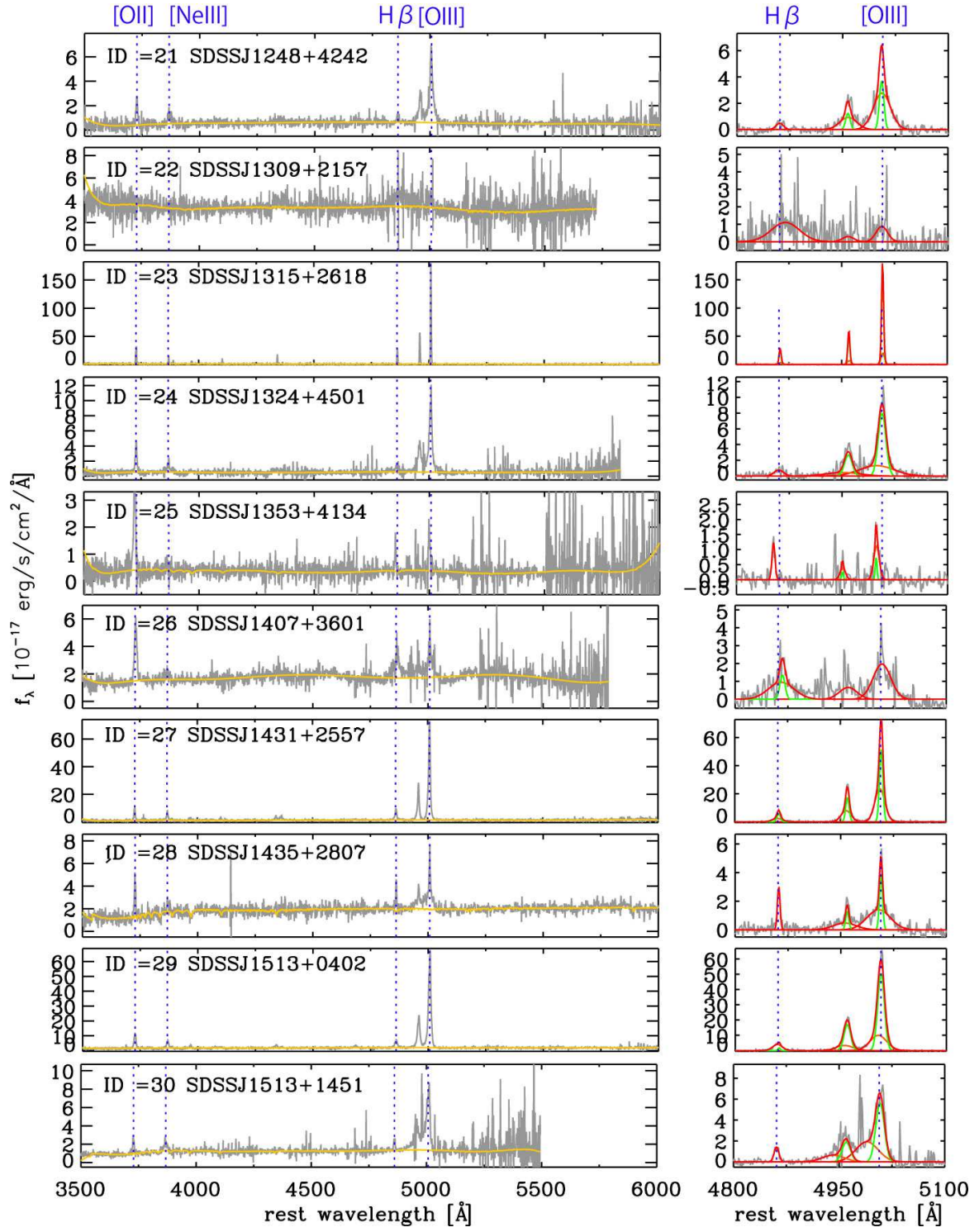


Figure A3. Same as Figure A1, but for DOGs with ID=21–30.

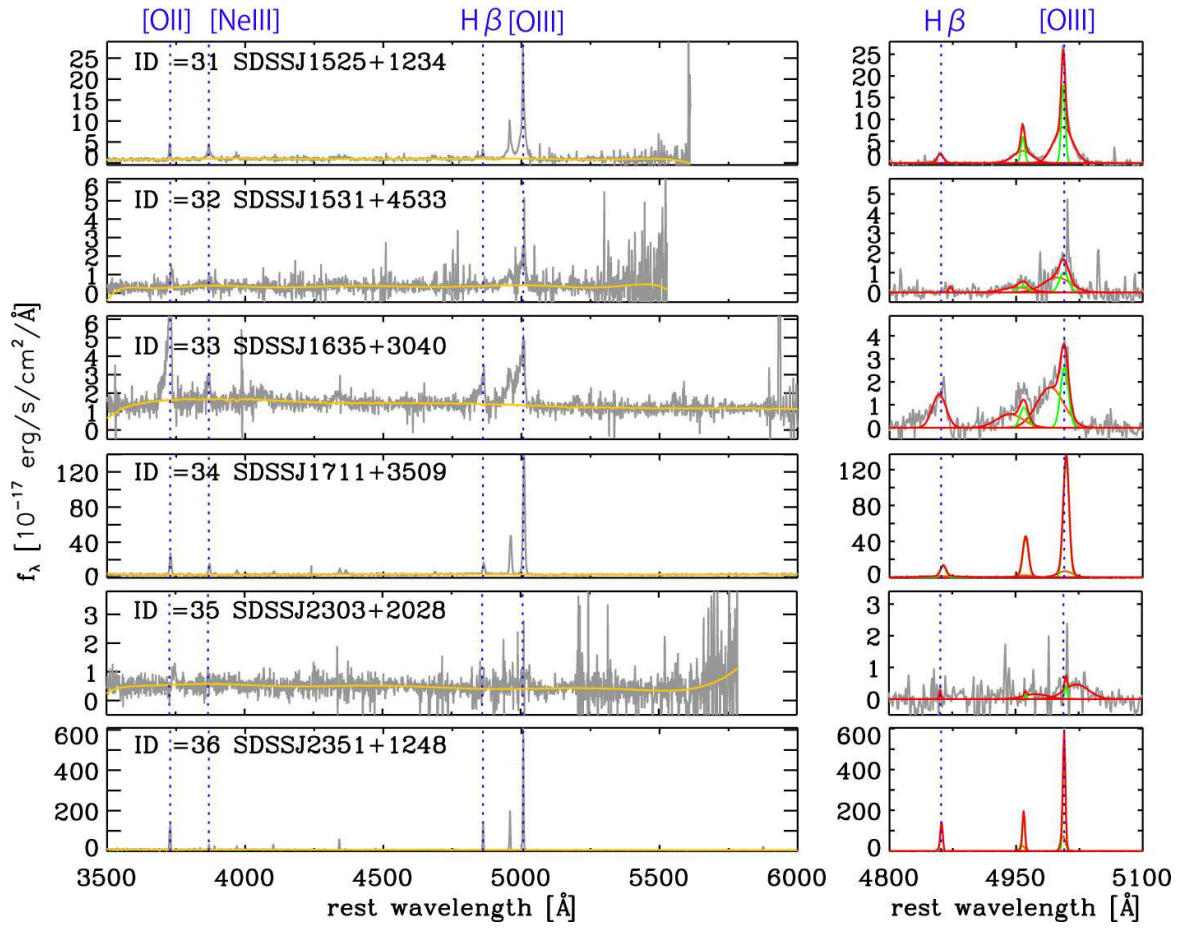


Figure A4. Same as Figure A1, but for DOGs with ID=31–36.

Table 1. [OIII] properties of WISE-SDSS spec DOGs.

ID	objname	R.A. ^a hms	Decl. ^a dms	Plate	fiberID	MJD	redshift	type ^b	$i - [22]$ AB mag	$\log L_{\text{IR}}^c$ L_{\odot}	$\log L_{\text{bol}}^d$ erg s ⁻¹	$w_{[\text{OIII}]}^e$	$v_{[\text{OIII}]}$ km/s	$\sigma_{[\text{OIII}]}$ km/s
1	SDSSJ0045+1339	00:45:29.1	+13:39:08.6	419	137	51879	0.295	type 2	7.11	10.70	44.58	1	16.8 ± 20.8	99.3 ± 3.5
2	SDSSJ0048-0046	00:48:46.4	-00:46:11.9	3590	256	55201	0.939	type 2	7.55	12.45	46.26	1	-1427.8 ± 191.5	1125.4 ± 80.2
3	SDSSJ0749+3353	07:49:34.6	+33:53:08.6	3751	813	55234	0.620	type 2	7.14	12.39	46.07	1	-151.3 ± 107.3	316.7 ± 136.9
4	SDSSJ0751+2958	07:51:20.5	+29:58:47.1	3752	435	55236	0.437	type 2	7.14	12.14	45.94	1	43.8 ± 27.6	230.6 ± 6.7
5	SDSSJ0756+4432	07:56:09.9	+44:32:22.8	6376	806	56269	0.510	type 2	7.18	12.39	46.22	1	-555.0 ± 88.9	978.6 ± 63.4
6	SDSSJ0819+4417	08:19:47.3	+44:17:22.8	6379	933	56340	0.578	type 2	7.28	12.38	46.22	1	-717.2 ± 130.8	777.2 ± 70.9
7	SDSSJ0832+4606	08:32:48.2	+46:06:02.6	5160	330	55895	0.721	type 2	7.10	11.90	45.73	0	-229.3 ± 500.1	801.5 ± 45.0
8	SDSSJ0833+4508	08:33:38.5	+45:08:33.5	7326	452	56710	0.925	type 2	7.05	12.15	46.04	1	-252.6 ± 38.0	360.9 ± 81.9
9	SDSSJ0847+4740	08:47:15.0	+47:40:14.0	7320	160	56722	0.713	type 2	7.39	12.10	45.88	1	-56.9 ± 36.3	290.5 ± 62.2
10	SDSSJ0919+5914	09:19:45.0	+59:14:30.9	5712	229	56602	0.829	type 2	7.22	12.68	46.34	1	-184.0 ± 199.2	536.3 ± 43.0
11	SDSSJ1009+4935	10:09:41.3	+49:35:26.5	7381	548	56717	0.308	type 2	7.19	11.23	44.90	0	5.6 ± 24.2	76.7 ± 0.6
12	SDSSJ1010+3725	10:10:34.2	+37:25:14.7	1426	110	52993	0.282	type 1	7.23	12.07	45.89	1	-613.6 ± 29.5	971.1 ± 6.7
13	SDSSJ1028+5011	10:28:01.5	+50:11:02.5	6694	430	56386	0.776	type 1	7.20	11.97	45.84	1	-11.9 ± 259.3	476.0 ± 45.4
14	SDSSJ1029+0501	10:29:05.9	+05:01:32.4	4772	617	55654	0.493	type 2	7.11	12.16	45.96	0	-1485.0 ± 207.7	986.9 ± 146.6
15	SDSSJ1042+2451	10:42:41.1	+24:51:07.0	6417	509	56308	1.026	type 2	7.02	12.40	46.29	1	-414.8 ± 311.8	489.2 ± 147.6
16	SDSSJ1057+3609	10:57:14.5	+36:09:03.3	4626	442	55647	0.885	type 2	7.06	12.28	46.06	0	761.0 ± 570.1	371.1 ± 271.4
17	SDSSJ1159+1100	11:59:15.3	+11:00:42.8	5388	398	55983	0.351	type 2	7.01	11.90	45.57	0	-255.5 ± 57.4	578.0 ± 46.0
18	SDSSJ1210+6105	12:10:56.9	+61:05:51.5	6972	272	56426	0.926	type 2	7.63	12.54	46.34	1	195.1 ± 133.3	583.4 ± 10.2
19	SDSSJ1212+1916	12:12:36.5	+19:16:23.7	5848	737	56029	0.620	type 2	7.37	12.37	46.19	1	-1.0 ± 48.8	695.9 ± 19.5
20	SDSSJ1235+4827	12:35:44.9	+48:27:15.4	6670	254	56389	1.023	type 2	7.50	13.06	46.70	1	-26.1 ± 150.3	834.7 ± 37.6
21	SDSSJ1248+4242	12:48:36.1	+42:42:59.3	4703	632	55617	0.682	type 2	7.11	11.85	45.66	1	-12.8 ± 130.5	632.1 ± 45.4
22	SDSSJ1309+2157	13:09:56.3	+21:57:00.8	2650	23	54505	0.609	type 1	7.49	12.06	45.88	0	-518.0 ± 348.2	485.5 ± 104.2
23	SDSSJ1315+2618	13:15:14.0	+26:18:41.3	2243	171	53794	0.305	type 2	8.03	10.93	44.77	1	12.4 ± 20.9	82.1 ± 2.6
24	SDSSJ1324+4501	13:24:40.1	+45:01:33.8	6625	124	56386	0.774	type 2	7.78	12.38	46.20	1	-118.1 ± 234.9	1009.2 ± 103.6
25	SDSSJ1353+4134	13:53:34.6	+41:34:39.0	6631	212	56364	0.686	type 2	7.43	12.29	45.93	1	67.2 ± 93.3	214.1 ± 44.9
26	SDSSJ1407+3601	14:07:44.0	+36:01:09.5	3854	24	55247	0.783	type 1	7.17	12.58	46.36	0	-257.5 ± 56.4	754.9 ± 43.4
27	SDSSJ1431+2557	14:31:36.4	+25:57:06.8	2135	482	53827	0.481	type 2	7.26	11.92	45.72	1	-63.2 ± 22.5	340.1 ± 4.3
28	SDSSJ1435+2807	14:35:40.3	+28:07:25.5	6018	975	56067	0.346	type 2	7.28	11.76	45.56	1	-208.7 ± 102.0	854.6 ± 92.2
29	SDSSJ1513+0402	15:13:33.8	+04:02:22.8	4776	25	55652	0.597	type 2	7.23	12.54	46.38	1	-121.1 ± 24.7	481.8 ± 6.2
30	SDSSJ1513+1451	15:13:54.4	+14:51:25.2	5486	200	56030	0.882	type 2	7.33	12.49	46.30	1	-539.3 ± 186.3	902.4 ± 141.3
31	SDSSJ1525+1234	15:25:04.7	+12:34:01.7	5492	818	56010	0.851	type 2	7.19	12.18	46.01	1	10.5 ± 45.9	562.5 ± 19.9
32	SDSSJ1531+4533	15:31:05.1	+45:33:03.4	6735	246	56397	0.871	type 2	7.47	12.20	46.05	1	-1009.2 ± 387.8	855.6 ± 152.5
33	SDSSJ1635+3040	16:35:59.3	+30:40:32.8	5202	322	55824	0.578	type 2	7.09	12.37	46.02	1	-515.7 ± 224.2	932.1 ± 100.7
34	SDSSJ1711+3509	17:11:45.7	+35:09:27.7	4994	525	55739	0.316	type 2	7.33	11.74	45.58	1	-5.2 ± 22.0	258.8 ± 5.2
35	SDSSJ2303+2028	23:03:01.6	+20:28:20.5	6121	70	56187	0.788	type 2	7.32	12.40	46.26	1	890.7 ± 467.9	857.3 ± 170.9
36	SDSSJ2351+1248	23:51:20.1	+12:48:19.9	6145	163	56266	0.052	type 2	7.11	10.52	44.21	1	-100.9 ± 20.5	99.6 ± 0.5

^a The coordinates in the SDSS DR12.

^b 1: type 1 AGN. 2: type 2 AGN (see Section 2).

^c The infrared luminosity at 8–1000 μm derived in Toba & Nagao (2016).

^d The bolometric luminosity calculated by integrating the best-fit SED template at wavelengths longward of Ly α (see Section 4.1).

^e 0: there is no broad wing of [O III] line. 1: there is broad wing of [O III] line (see Section 3.1).